Response to the comments on the paper by Referee 1

Semi-Annual Variation of Excited Hydroxyl Emission at Mid-Latitudes

By Mykhaylo Grygalashvyly, Alexander I. Pogoreltsev, Alexey B., Andreyev, Sergei P.

Smyshlyaev, and Gerd R. Sonnemann

We appreciate the reviewer's constructive comments and positive judgment on our paper. We have taken the reviewer's suggestions into account when preparing the revised version of our manuscript.

In the following we address the comments of the reviewer point by point.

1. The data of observations represent nightly mean values averaged over years 2010-2017. We add such notation at line 93 of the revised manuscript: "The analysis presented in this paper uses data averaged over the years 2010-2017."
2. Following by your suggestion the labels (months) of Figures 2 and 3 were corrected.

Other changes are related to the recommendations and demands of other referee.

Thank you for taking the time to review our manuscript.

With respect,

Mykhaylo Grygalashvyly, Alexander Pogoreltsev, Alexey Andreyev, Sergei Smyshlyaev, and

Gerd Reinhold Sonnemann

Response to the comments on the paper by Referee 2

Semi-Annual Variation of Excited Hydroxyl Emission at Mid-Latitudes

By Mykhaylo Grygalashvyly, Alexander I. Pogoreltsev, Alexey B., Andreyev, Sergei P.

Smyshlyaev, and Gerd R. Sonnemann

Dear Referee,

We appreciate positive judgment on our paper, constructive comments, and not formal approach to the review. We have taken your suggestions into account when preparing the revised version of our manuscript. In following we mention point by point how the manuscript has been changed according to your suggestions.

1. We add it at line 93 of the revised manuscript: "The analysis presented in this paper uses data averaged over the years 2010-2017."

2. We add the explanation at lines 113-115 of the revised manuscript: "We calculates volume emission for transition $OH^*_{v=6} \rightarrow OH^*_{v=2}$ as the product of the Einstein coefficient for given transition by concentration of excited hydroxyl at corresponding vibrational number, i.e. $V_{62} = E_{62}[OH^*_6]$."

3. We add such description at lines 136-141 of the revised manuscript, as well necessary references in the reference list:" This run is based on the dynamics and temperature of LIMA (Leibniz Institute Middle Atmosphere) model for the so-called "realistic case", in which carbon dioxide, ozone, and Lyman-α flux are taken from observations, and the horizontal winds and temperature of ECMWF (European Centre for Medium-Range Weather Forecasts) are assimilated below ~35 km (Berger, 2008; Lübken et al., 2009, 2013)."

4. We add such a comment at lines 133-135:" (the choice of this year does not affect our conclusions because calculations for other years show similar semi-annual variations)".

5. We add such notation at lines 159-162: "Note, that the observed intensity is directly proportional to the vertical integral of the volume emissions; hence, they reveal similar

64 variations and dependencies on surrounding conditions near the peak of the excited hydroxyl

65 layer."

66

67 6. We add such statements ant lines 156-157: "because we display monthly mean values and

68 standard deviations commonly exceed the errors of measurements".

69

70 7. Following by your suggestion we add Eq. (A6) into the Section 3 with explanations about

71 mean states and perturbations, as well we modified the description of the Fig. 3:" In order to

72 assess the input into annual variability from different sources, we calculate relative to annual

73 averaged variations of volume emissions due to atomic oxygen, temperature, and air density

74 ~~(Eq. A6)~~:

$$RD'_O = 100\% \cdot \frac{V'_O}{\overline{V}} = 100\% \cdot \frac{[O]'}{\overline{[O]}},$$

75 $$RD'_T = 100\% \cdot \frac{V'_T}{\overline{V}} = 100\% \cdot -2.4\frac{T'}{\overline{T}}, \qquad (2)$$

$$RD'_M = 100\% \cdot \frac{V'_M}{\overline{V}} = 100\% \cdot \frac{[M]'}{\overline{[M]}},$$

76 where overbar denotes annually averaged values and prime denotes difference of actual

77 (modeled or observed) values from annually averaged (in our case this is difference between

78 nightly mean one month sliding averaged values (Fig. 2) and nightly mean annually averaged

79 values)."

80 We did not add the equation (A7) because second momentum have not essential impact on

81 volume emission variability and in future investigations their consideration could be omitted.

82

83 Technical comments:

84

85 Line 86. This technical but very large problem was comprehensively described in large

86 number of works of Lopez-Gonzalez, which we refer in our reference list.

87

88 Part 2.2. Following by your suggestion, we collected description of coefficients for Eq. (1) in

89 the Table (1) and add in the text at lines 116-118 of the revised mynuscript: "All reactions

90 used in Eq. (1) and in appendix, together with corresponding reaction rates, branching ratios,

91 quenching rates and spontaneous emission coefficients, besides those for multi-quantum

92 processes, are collected in Table 1."

93

94 **Table 1**. List of reactions with corresponding reaction rates (for three-body reactions [cm^6

95 $molecule^{-2}$ s^{-1}] and for two-body reactions [cm^3 $molecule^{-1}$ s^{-1}]), branching ratios, quenching

96 coefficients, and spontaneous emission coefficients (s^{-1}) used in the paper.

	Reaction	Coefficient/branching ratios	Reference
1	$H + O_3 \xrightarrow{\varsigma_v a_1} OH_{v=5,\dots,9} + O_2$	$a_1 = 1.4 \cdot 10^{-10} exp\left(\dfrac{-470}{T}\right)$ $\varsigma_{v=9,\dots,5} = 0.47, 0.34, 0.15, 0.03, 0.01$	Burkholder et al. (2015), Adler-Golden (1997)
2	$O + HO_2 \xrightarrow{\psi_v a_2} OH_{v=5,\dots,9} + O_2$	$a_2 = 3.0 \cdot 10^{-11} exp\left(\dfrac{200}{T}\right)$ $\psi_{v=3,\dots,1} = 0.1, 0.13, 0.34$	Burkholder et al. (2015), Kaye (1988), Takahashi and Batista (1981)
3	$O + OH_{v=1,..,9} \rightarrow O_2 + H$	$a_3(v = 9, \dots, 5) = (5.07, 4.52, 3.87, 3.93, 3.22, 3.68, 3.05, 3.19, 3,42) \cdot 10^{-11}$	Varandas (2004), Caridade et al. (2013)
4	$O + O_2 + M \rightarrow O_3 + M$	$a_4 = 6 \cdot 10^{-34}(300/T)^{2.4}$	Burkholder et al. (2015)
5	$O + O_3 \rightarrow 2O_2$	$a_5 = 8 \cdot 10^{-12} exp\left(\dfrac{-2060}{T}\right)$	Burkholder et al. (2015)
6	$OH_v + O_2, O, N_2 \rightarrow OH_{v'<v} + O_2, O, N_2$	$B_{vv\prime}, D_{vv\prime}, C_{vv\prime}$	Adler-Golden (1997), Caridade et al. (2013), Makhlouf et al. (1995)
7	$OH_v \rightarrow OH_{v'<v} + hv$	$E_{vv\prime}$	Xu et al. (2012)

97

98

99 Line 600. Thank you for this note, it is true. We corrected the description of the Fig. 1.

100

101 Figures 2 and 3. We changed the time scale of these figures according with your suggestion.

102

103 Line 83. We change this nomenclature according with common nomenclature of our

104 manuscript.

105

106 All of your language and stile corrections at lines 167, 171, 179, 200, 232, and 249-250 were

107 applied completely.

108

109 Other changes are related to the recommendations and demands of other referee.

110 Thank you for taking the time to review our manuscript.

111

With respect,

Mykhaylo Grygalashvyly, Alexander Pogoreltsev, Alexey Andreyev, Sergei Smyshlyaev, and

Gerd Reinhold Sonnemann

139 **Semi-Annual Variation of Excited Hydroxyl Emission at Mid-Latitudes**

140 Mykhaylo Grygalashvyly[1], Alexander I. Pogoreltsev[2], Alexey B., Andreyev[3], Sergei P.

141 Smyshlyaev[2], and Gerd R. Sonnemann[1]

142 [1]Leibniz-Institute of Atmospheric Physics at the University Rostock in Kühlungsborn,

143 Schloss-Str.6, D-18225 Ostseebad Kühlungsborn, Germany

144 [2]Department of Meteorological Forecasting, Russian State Hydrometeorological University

145 (RSHU), Saint-Petersburg, Russia

146 [3]Institute of the Ionosphere, Almaty, Kazakhstan

147

148 **Abstract**

149 Ground-based observations show a phase shift in semi-annual variation of excited hydroxyl

150 (OH*) emissions at mid-latitudes (43° N) compared to those at low latitudes. This differs

151 from the annual cycle at high latitudes. We examine this behaviour utilising an OH* airglow

152 model which was incorporated into the 3D chemistry-transport model (CTM). Through this

153 modelling, we study the morphology of the excited hydroxyl emission layer at mid-latitudes

154 (30° N -50° N), and we assess the impact of the main drivers of its semi-annual variation:

155 temperature, atomic oxygen, and air density. We found that this shift in the semi-annual cycle

156 is determined mainly by the superposition of annual variations of temperature and atomic

157 oxygen concentration. Hence, the winter peak for emission is determined exclusively by

158 atomic oxygen concentration, whereas the summer peak is the superposition of all impacts,

159 with temperature taking a leading role.

160

161 **1. Introduction**

162

163 Since the second half of the 20th century, emissions of excited hydroxyl have been

164 used for three main purposes: 1) to infer information about temperature and its long-term

6

change; 2) to obtain distributions of minor chemical constituents (O_3, H, and O) at the altitudes of the mesopause; and 3) to investigate dynamic processes such as tides, gravity, and planetary waves (GWs and PWs, respectively), sudden stratospheric warmings (SSWs), and quasi-biennial oscillation (QBO).

Hence, a number of authors have studied temperatures in the mesopause region using airglow emission ground-based observations focusing on long-term trends (e.g., Bittner et al., 2002; Holmen et al., 2014; Dalin et al., 2020, and references therein) with attention to seasonal variations (e.g., Reid et al., 2017, and references therein) and the solar-cycle effect (e.g., Kalicinsky et al., 2016, and references therein).

Minor chemical constituents as well as chemical heat have also been retrieved by OH* emission observations. Ever since atomic oxygen concentration was determined by the rocket-born detection of OH* airglow (Good, 1976), this method has come into wide use for obtaining information about distributions of minor chemical constituents in the mesopause region, namely, atomic oxygen concentration (e.g., Russell et al., 2005; Mlynczak et al., 2013a, and references therein), ozone concentration (e.g., Smith et al., 2009, and references therein), atomic hydrogen concentration (e.g., Mlynczak et al., 2014, and references therein), and exothermic chemical heat (e.g., Mlynczak et al., 2013b, and references therein). In future, excited hydroxyl airglow could be used for measurements of hydroperoxy radicals and water vapor concentrations (Kulikov et al., 2009, 2018; Belikovich et al., 2018).

Numerous works using airglow observations, have been devoted to dynamic processes, for example, to study mesopause variabilities in time of SSWs (Damiani et al., 2010; Shepherd et al., 2010). Gao et al. (2011) studied the temporal evolution of nightglow brightness and height during SSW events. A year earlier, they found a QBO signal in the excited hydroxyl emission (Gao et al., 2010). The climatology of PWs was investigated in works by Takahashi et al. (1999), Buriti et al. (2005), and Reisin et al. (2014). Tides were studied by Xu et al. (2010) and Lopez-Gonzalez et al. (2005). GW parameters based on the airglow technique were

investigated, for example, by Taylor et al. (1991) and Wachter et al. (2015). A more complete description of works in which hydroxyl emissions were used to study dynamic processes can be found in a review by Shepherd et al. (2012).

The morphology of the OH* layer is an essential component in the interpretation of observations and in understanding the processes involved in layer variability. Annual variations in the OH* layer have been identified at all latitudes (Marsh et al., 2006). Equatorial and low-latitude semi-annual variations have been observed by satellites (e.g., Abreu and Yee, 1989; Liu et al., 2008, and references therein), as well as by ground-based instruments (Takahashi et al., 1995), and they have been modelled by several research teams (Le Texier et al., 1987; Marsh et al., 2006, and references therein). The maxima of emissions were found to occur near equinoxes. In spite of the large number of studies on this subject, there are still knowledge gaps. Recently, unexpected behaviour in the semi-annual cycle of excited hydroxyl emission has been found by ground-based observations, with a shift of the peaks from equinoxes to summer and winter at middle latitudes (Popov et al., 2018; Popov et al., 2020); this was also found by modelling (Grygalashvyly et al., 2014, Fig. 3). Similar variations in OH* emissions with peaks near equinoxes have been observed at middle latitudes (34.6° N) in the southern hemisphere (Reid et al., 2014). These results were provided without explanations; in our short paper, we offer a preliminary explanation.

The second chapter of our manuscript describes the observational technique and model that were applied; in the third chapter, we present results and an analysis of observations and modelling; conclusions are provided in the fourth chapter.

2. Observational technique and model

2.1. Observational technique

The spectral airglow temperature imager (SATI), which measures nightglow intensity for vibrational transitions of $OH^*_{v=6} \rightarrow OH^*_{v=2}$ and temperature using vibrational-rotational transitions, was assembled at the Institute of Ionosphere (43° N, 77° E) in Almaty, Kazakhstan. It represents a Fabry-Perot spectrometer with a CCD (charge-coupled device) camera as a detector and a narrow-band interference filter as the etalon. Following Lopez-Gonzalez et al. (2007), we use an interference filter with the centre at 836.813 nm and a bandwidth of 0.182 nm. This corresponds to the spectral region of the OH*(6-2) $OH^*_{v=6} \rightarrow OH^*_{v=2}$ band. In order to infer the temperature, the calculated spectra for different vibro-rotational transitions are compared with those from observations. The SATI operates at a sixty-second exposure that provides corresponding time resolution. The method of temperature retrieval is well-described by Lopez-Gonzalez et al. (2004). The observations of temperature were validated using satellite SABER measurements (Lopez-Gonzalez et al., 2007; Pertsev et al., 2013). Additional details about this instrument are presented in many papers (Wies et al., 1997; Aushev et al., 2000; Lopez-Gonzalez et al., 2004, 2005, 2007, 2009). The analysis presented in this paper uses data averaged over the years 2010-2017.

2.2. Model and numerical experiment

The model of excited hydroxyl (MEH) calculates the OH* number densities at each vibrational level v as the production divided by losses (excited hydroxyl is assumed in the photochemical equilibrium), which include the chemical sources as well as collisional and emissive removal:

$$[OH_v] = \frac{\left(\begin{matrix} \varsigma_v a_1 [O_3][H] + \psi_v a_2 [O][HO_2] + \sum_{v'=v+1}^{9} B_{v'v}[O_2][OH_{v'}] + C_{v+1}[N_2][OH_{v+1}] + \\ + \sum_{v'=v+1}^{9} D_{v'v}[O][OH_{v'}] + \sum_{v'=v+1}^{9} E_{v'v}[OH_{v'}] \end{matrix} \right)}{\left(\begin{matrix} a_3(v)[O] + \sum_{v''=0}^{v-1} D_{vv''}[O] + C_v[N_2] + \\ + \sum_{v''=0}^{v-1} B_{vv''}[O_2] + \sum_{v''=0}^{v-1} E_{vv''} \end{matrix} \right)}, \begin{pmatrix} v < v' \\ v'' < v \end{pmatrix}. \qquad (1)$$

240 The first term in the numerator of (1) is the reaction $O_3 + H \rightarrow OH_v + O$, where a_1 is the

241 reaction rate, and ς_v represents the branching ratios (Adler-Golden, 1997). The second term is

242 the $O + HO_2 \rightarrow OH_v + O_2$ reaction, where a_2 and ψ_v are the reaction rate and nascent

243 distribution, respectively (Kaye (1988) after Takahashi and Batista (1981)). The other three

244 summands represent the populations resulting from collisional relaxation from higher *v*-

245 levels, where *B*, *C*, and *D* are the collisional deactivation coefficients for O_2 (Adler-Golden,

246 1997), N_2 (Makhlouf et al., 1995), and O (Caridade et al., 2013), respectively. The last

247 summand is the multi-quantum population by spontaneous emissions, where $E_{v'v}$ is the

248 spontaneous emission coefficient (Xu et al., 2012). The losses occur, additionally, through the

249 chemical removal of the excited hydroxyl by atomic oxygen, where $a_3(v)$ is the vibrationally

250 dependent reaction rate (Varandas, 2004). The calculations in Eq. (1) are incorporated into the

251 chemistry-transport model (CTM). We calculates volume emission for transition

252 $OH^*_{v=6} \rightarrow OH^*_{v=2}$ as the product of the Einstein coefficient for given transition by

253 concentration of excited hydroxyl at corresponding vibrational number, i.e. $V_{62} = E_{62}[OH^*_6]$.

254 All reactions used in Eq. (1) and in appendix, together with corresponding reaction rates,

255 branching ratios, quenching rates and spontaneous emission coefficients, besides those for

256 multi-quantum processes, are collected in Table 1.

257 Here, we enumerate only the main features of the CTM as one can find extended descriptions

258 in manyworks (Sonnemann and Grygalashvyly, 2020; Grygalashvyly et al., 2014; and

259 references therein). The CTM consists of four blocks: chemical, transport, radiative, and

260 diffusive. The chemical block accounts for 19 constituents, and 63 photo-dissociations and

261 chemical reactions (Burkholder et al., 2015). The chemical code utilises a family approach

262 with the odd-oxygen ($O(^1D)$, O, O_3), odd-hydrogen (H, OH, HO_2, H_2O_2), and odd-nitrogen

263 ($N(^2D)$, $N(^4S)$, NO, NO_2) families (Shimazaki, 1985). In the radiative part, the dissociation

264 rates are taken from a pre-calculated table depending on zenith angle and altitude (Kremp et

265 al., 1999). The transport block calculates advections in three directions following Walcek

(2000). The diffusive part accounts for only vertical molecular plus turbulent diffusion (Morton and Mayers, 1994). This model has been validated against observations of ozone, which plays a role in the formation of OH* (e.g., Hartogh et al., 2011; Sonnemann et al., 2007; and references therein) and water vapour, which is the principal source of odd-hydrogens and, particularly, of atomic hydrogen (e.g., Hartogh et al., 2010; Sonnemann et al., 2008; and references therein). Our current analysis used the run for year 2009 (the choice of this year does not affect our conclusions because calculations for other years show similar semi-annual variations), which was published and described in a number of works (Grygalashvyly et al., 2014, section 4; Sonnemann et al., 2015). This run is based on the dynamics and temperature of LIMA (Leibniz Institute Middle Atmosphere) model for the so-called "realistic case", in which carbon dioxide, ozone, and Lyman-α flux are taken from observations, and the horizontal winds and temperature of ECMWF (European Centre for Medium-Range Weather Forecasts) are assimilated below ~35 km (Berger, 2008; Lübken et al., 2009, 2013).

Here we assume that the structures in the longitudinal direction are equivalent to local time (LT) behaviour, with 24 LT related to midnight at 0° longitude. The LTs of successive longitudes are used to analyse our calculations. Hence, in the following figures related to the model results, longitude is used as the so-called 'pseudo time'. The night-time averaged values account for the period from 21:45 LT to 2:15 LT. For the purposes of our discussion, we use 'pressure-altitude' (or other words 'pseudo-altitude') $Z^* = -H \ln(P/P_0)$, where P represents pressure: $P_0 = 1013 \, mbar$ is the surface pressure, and $H = 7 \, km$ is the scale height.

3. Results and discussion

291   Figure 1a illustrates the nightly mean monthly averaged values of the observed annual

292   variability of intensity at 43° N (red line) and the modelled annual variability of volume

293   emission at the peak of the OH* layer at 43.75° N (black line), both for transition

294    $OH^*_{v=6} \rightarrow OH^*_{v=2}$. The error bar shows monthly standard deviation, because we display

295   monthly mean values and standard deviations commonly exceed the errors of measurements.

296   By the observations as well as by modelling, we can clearly see semi-annual variations of

297   emissions with peaks in winter and summer. Note, that the observed intensity is directly

298   proportional to the vertical integral of the volume emissions; hence, they reveal similar

299   variations and dependencies on surrounding conditions near the peak of the excited hydroxyl

300   layer.

301   Grygalashvyly et al. (2014), Sonnemann et al. (2015), and Grygalashvyly (2015) have derived

302   and confirmed through modelling that the concentration of excited hydroxyl (hence, volume

303   emission and intensity) at peak is directly proportional to the product of the surrounding

304   pressure (hence, it depends on altitude), atomic oxygen number density, and the negative

305   power of temperature (Eq. A2 in the Appendix). Thus, in order to infer the reasons for this

306   semi-annual variation, one should consider three drivers of OH* variability: temperature,

307   atomic oxygen concentration, and height of the layer.

308   Figure 1b shows the monthly mean nightly averaged values of the observed annual variability

309   of temperature at 43° N (red line) and the modelled annual variability of temperature at the

310    $OH^*_{v=6}$ peak at 43.75° N (black line). Both the observations and the modelling show minima

311   in summer and maxima in winter. Hence, the temperature decline can be one of the reasons

312   for the summer intensity (and volume emission) peak.

313   Figures 1c and 1d depict modelled monthly mean nightly averaged values of atomic oxygen at

314    $OH^*_{v=6}$ peak and the height of the excited hydroxyl peak, respectively, at 43.75° N. The

315   modelling shows the peaks of atomic oxygen concentration in July and December–January,

316   with the largest values in winter. The variation of height through the year occurs from ~90 km

317   to 94 km. This is an essential variability and provides input to the variability of the

318   concentration of the surrounding air.

319   In order to study the morphology of this semi-annual variation and assess the impacts of

320   temperature, atomic oxygen concentration, and height (concentration of air) variability, we

321   calculate one-month sliding averaged values based on the model results. Figure 2 illustrates

322   the modelled annual variability at the $OH^*_{v=6}$ peak: a) volume emission ($OH^*_{v=6} \rightarrow OH^*_{v=2}$), b)

323   temperature, c) atomic oxygen concentration, and d) height of the peak.

324   The summer maximum of volume emission (Fig. 2a) shows the strongest values in July and is

325   extended from ~30° N to ~50° N. The summer maximum is stronger than that in winter. The

326   winter maximum has its strongest values in January and a positive gradient into the winter

327   pole direction; at latitudes 30°–50° N, it represents the ~~rest~~ part of the annual variation at high

328   latitudes that occurs because of the annual variation in general mean circulation and fluxes of

329   atomic oxygen which correspond to this variability (Liu et al., 2008; Marsh et al., 2006).

330   Similar behaviour of the emissions for transition $OH^*_{v=8} \rightarrow OH^*_{v=3}$ was captured by WINDII

331   (Wind Imaging Interferometer) and modelled by Thermosphere-Ionosphere-Mesosphere

332   Electrodynamics General Circulation Model at 84–88 km (Liu et al., 2008, Fig. 5 and 6).

333   The temperature (Fig. 2b) shows a clear annual variation from the middle to the high

334   latitudes, with a minimum ~150 K at middle latitudes in July. The summer minimum at the

335   middle latitudes is ~~an~~ the echo of ~~those~~ the one at high latitudes. The atomic oxygen

336   concentrations (Fig. 2c) reveal the annual cycle. The concentrations have a maximum in

337   winter and a minimum in summer at high and middle latitudes, as has already been observed

338   (Smith et al., 2010). However, in the region from ~30° to ~50° N in summer, atomic oxygen

339   concentrations show one additional peak in June–July. Formation of this summer peak can be

340   explained by the transformed Eulerian mean (TEM) circulation (Limpasuvan et al., 2012, Fig.

341   7; Limpasuvan et al., 2016, Fig. 5), which brings into the summer hemisphere the air reached

342   by atomic oxygen from the region of its production at high latitudes above 100 km to ~90 km

343 at ~30°–50° N. The peak altitude of the $OH^*_{v=6}$ (Fig. 2d) shows complex annual variability.

344 There is a secondary maximum OH* peak at ~30°–50° N in summer.

345 In order to assess the input into annual variability from different sources, we calculate relative

346 to annual averaged variations of volume emissions due to atomic oxygen, temperature, and air

347 density (Eq. A6):

$$
\begin{aligned}
RD'_O &= 100\% \cdot \frac{V'_O}{\overline{V}} = 100\% \cdot \frac{[O]'}{\overline{[O]}}, \\
RD'_T &= 100\% \cdot \frac{V'_T}{\overline{V}} = 100\% \cdot -2.4\frac{T'}{\overline{T}}, \\
RD'_M &= 100\% \cdot \frac{V'_M}{\overline{V}} = 100\% \cdot \frac{[M]'}{\overline{[M]}},
\end{aligned}
\tag{2}
$$

349 where overbar denotes annually averaged values and prime denotes difference of actual

350 (modeled or observed) values from annually averaged (in our case this is difference between

351 nightly mean one month sliding averaged values (Fig. 2) and nightly mean annually averaged

352 values). The derivation of these parameters is presented in the appendix. A similar approach

353 can be useful for analysing emission variations due to GWs, PWs, and tides.

354 Figure 3a shows relative variations of emissions due to impacts of atomic oxygen (black line),

355 temperature (red line), and air density (green line) at 43.75° N. The strongest emission

356 variation occurs because of changes in atomic oxygen concentration: the amplitude of its

357 relative deviation amounts to ~50%. The amplitudes of relative deviations of emissions due to

358 temperature and air density amount to ~15% and ~20%, respectively. The atomic oxygen

359 variation gives the most essential input into the winter maximum of emission (black line).

360 Because of the downward transport of atomic oxygen in winter, the volume emission rises by

361 ~50% of annual average averaged annually. The summer maximum is determined by the

362 superposition of all three factors. After the spring reduction of emissions due to the decline of

363 atomic oxygen concentration (~-40% of annual averaged values), the emissions rise again to

364 approximately the annual average values in June–July. This is synchronised with the growth

365 of volume emissions by ~20% over the annual average values due to summer temperature

14

declines (red line) and with the growth of volume emissions by ~15% over the annual average due to the decline of peak altitude in April–September and the corresponding rise of air density (green line).

Figure 3b illustrates relative variations of emissions due to second momenta (Eq. A7 in the Appendix). The second momenta do not provide essential input to annual variation. The strongest among them, $\frac{[O]'M'}{\overline{[O]}\,\overline{M}}$ (blue line), gives emission variability with an amplitude ~6% of annual averaged values.

In the context of our short paper, the ultimate question regarding the role of tides and GWs on semi-annual variations of OH* emissions at middle latitudes has not been answered. Undoubtedly, the simultaneous analysis of observations of excited hydroxyl emissions from several stations is desirable to explore this question.

4. Summary and conclusions

Based on observations and numerical simulation, we confirmed the existence of a semi-annual cycle of excited hydroxyl emission at middle latitudes with maxima in summer (June–July) and winter (December–January). The annual variation in general mean circulation and atomic oxygen concentration corresponding to the excited hydroxyl emission cycle was found to be the leading cause of the winter maximum of this cycle, whereas the summer maximum represents the superposition of three different processes: atomic oxygen meridional transport due to residual circulation from the summer pole to the equator; temperature decline, which represents the rest of the mesopause cooling at summer high latitudes; and air concentration growth at the peak of the excited hydroxyl emission layer due to hydroxyl layer descent at middle latitudes in April–September.

15

Appendix.

To obtain the derivation of Eq. (2), we start with a simplified equation for excited hydroxyl concentration. Taking into account that the ozone is in photochemical equilibrium in the vicinity of the $[OH_v]$ layer and above during night-time (Kulikov et al., 2018; Belikovich et al., 2018; Kulikov et al., 2019); utilising the equation for ozone balance during night-time $(a_5[O_3][O] + a_1[H][O_3] = a_4[O][O_2][M])$, where a_4 and a_5 are the coefficients for the corresponding reactions; omitting the reaction of atomic oxygen with ozone as relatively slow (Smith et al., 2008); substituting the reduced ozone balance equation for the excited hydroxyl balance equation (first term in the numerator of Eq. (1)); assuming that the most effective production of excited hydroxyl occurs due to the reaction of ozone with atomic hydrogen and that the most effective losses are due to quenching with molecular oxygen; we obtain from Eq. (1) a simplified expression in which excited hydroxyl concentration is represented in terms of atomic oxygen concentration, temperature (in a_4), and concentration of the surrounding air:

$$[OH_v] \approx \mu_v a_4[O][M]. \tag{A1}$$

Here $\mu_v = \frac{\varsigma_v + \sum_{v'=v+1}^{v'=9} \mu_{v'} B_{v'v}}{\sum_{v''=0}^{v''=v-1} B_{vv''}}$, $(\varsigma_{v>9} = 0)$ are the coefficients representing the arithmetic combination of branching ratios ς_v and quenching coefficients $B_{v'v}$. More comprehensive derivations of (A1) can be found in a number of papers (Grygalashvyly et al., 2014; Grygalashvyly, 2015; Grygalashvyly and Sonnemann, 2020). Although ~~this is too simplified to be used for precise~~ the accuracy of (A1) estimate is insufficient for model calculations, it is useful for obtaining information about impacts and for assessing variabilities.

By multiplying (A1) by the Einstein-coefficient $E_{vv''}$ for given a transition, writing the reaction rate explicitly $a_4 = 6 \cdot 10^{-34}(300/T)^{2.4}$ (Burkholder et al., 2015), and collecting all

415   constants in $\chi_{vv''}$, we obtain an expression for volume emission in terms of atomic oxygen

416   concentration, temperature, and air number density:

417    $$V \approx \chi_{vv''} T^{-2.4}[O][M],\qquad (A2)$$

418   where $\chi_{vv''} = \mu_v E_{vv''} \cdot 6 \cdot 10^{-34} \cdot 300^{2.4}$.

419   Next, we apply Reynolds decomposition by averaged and variable part to the temperature,

420   atomic oxygen concentration, and concentration of air in (A2):

421    $$V \approx \chi_{vv''} (\bar{T} + T')^{-2.4}(\overline{[O]} + [O]')(\overline{[M]} + [M]'),\qquad (A3)$$

422   where $\bar{T}$, $\overline{[O]}$, $\overline{[M]}$ are average parts, and T', $[O]'$, $[M]'$ are the corresponding varying parts.

423   After decomposing the term with temperature in the Taylor expansion and cross-multiplying

424   all terms of (A3), we obtain:

425    $$V \approx \chi_{vv''} \bar{T}^{-2.4}\overline{[O]} \cdot \overline{[M]} + \chi_{vv''} \bar{T}^{-2.4}\overline{[O]}[M]' + \chi_{vv''} \bar{T}^{-2.4}[O]'\overline{[M]} - 2.4\chi_{vv''} T'\bar{T}^{-3.4}\overline{[O]} \cdot$$

426    $$\overline{[M]} + \chi_{vv''} \bar{T}^{-2.4}[O]'[M]' - 2.4\chi_{vv''} T'\bar{T}^{-3.4}\overline{[O]}[M]' - 2.4\chi_{vv''} T'\bar{T}^{-3.4}[O]'\overline{[M]} -$$

427    $$2.4\chi_{vv''} T'\bar{T}^{-3.4}[O]'[M]'.\qquad (A4)$$

428   The volume emission for a given transition can be represented as follows:

429    $$V \approx \bar{V} + V'_M + V'_O + V'_T + V''_{OM} + V''_{TM} + V''_{TO} + higher\ momenta,\qquad (A5)$$

430   where, $\bar{V} = \chi_{vv''} \bar{T}^{-2.4}\overline{[O]} \cdot \overline{[M]}, V'_M = \chi_{vv''} \bar{T}^{-2.4}\overline{[O]}[M]', V'_O = \chi_{vv''} \bar{T}^{-2.4}[O]'\overline{[M]}, V'_T =$

431    $-2.4\chi_{vv''} T'\bar{T}^{-3.4}\overline{[O]} \cdot \overline{[M]}, V''_{OM} = \chi_{vv''} \bar{T}^{-2.4}[O]'[M]', V''_{TM} =$

432    $-2.4\chi_{vv''} T'\bar{T}^{-3.4}\overline{[O]}[M]', V''_{TO} = -2.4\chi_{vv''} T'\bar{T}^{-3.4}[O]'\overline{[M]}$.

433   Hence, relative deviations (RD) of emissions due to variations in atomic oxygen, temperature,

434   and concentration of air are:

435
$$
\begin{aligned}
RD'_O &= 100\% \cdot \frac{V'_O}{\bar{V}} = 100\% \cdot \frac{[O]'}{\overline{[O]}}, \\
RD'_T &= 100\% \cdot \frac{V'_T}{\bar{V}} = 100\% \cdot -2.4\frac{T'}{\bar{T}}, \qquad (A6) \\
RD'_M &= 100\% \cdot \frac{V'_M}{\bar{V}} = 100\% \cdot \frac{[M]'}{\overline{[M]}}.
\end{aligned}
$$

436   The relative deviations (RD) of emissions due to second momenta are

$$RD''_{OM} = 100\% \cdot \frac{V''_{OM}}{\bar{V}} = 100\% \cdot \frac{[O]'[M]'}{\overline{[O][M]}},$$

437
$$RD''_{TM} = 100\% \cdot \frac{V''_{TM}}{\bar{V}} = 100\% \cdot -2.4 \frac{T'[M]'}{\bar{T}\overline{[M]}}, \qquad (A7)$$

$$RD''_{TO} = 100\% \cdot \frac{V''_{TO}}{\bar{V}} = 100\% \cdot -2.4 \frac{T'[O]'}{\bar{T}\overline{[O]}}.$$

438

441 **Author contributions.** All authors contributed equally to this paper.

442 **Competing interests.** The authors declare that they have no conflict of interest.

448

449 **References**

450

451 Abreu, V. J., and Yee, J. H.: Diurnal and seasonal variation of the nighttime OH (8-3)

452 emission at low latitudes, J. Geophys. Res., 94(A9), 11949-11957, doi:10.1029/89JA00619,

453 1989.

454

455 Adler-Golden, S.: Kinetic parameters for OH nightglow modeling consistent with recent

456 laboratory measurements, J. Geophys. Res., 102(A9), 19969–19976, doi:10.1029/97JA01622,

457 1997.

458

459   Aushev, V. M., Pogoreltsev, A. I., Vodyannikov, V. V., Wiens, R. H., and Shepherd, G. G.:

460   Results of the airglow and temperature observations by MORTI at the Almaty site (43.05 N,

461   76.97 E), Phys. Chem. Earth, 25(5–6), 409–415, doi:10.1016/S1464-1909(00)00035-6, 2000.

462

463   Belikovich, M. V., Kulikov, M. Yu., Grygalashvyly, M., Sonnemann, G. R., Ermakova, T. S.,

464   Nechaev, A. A., and Feigin, A. M.: Ozone chemical equilibrium in the extended mesopause

465   under the nighttime conditions. Adv. Space Res., 61, 426-432, doi:10.1016/j.asr.2017.10.010,

466   2018.

467

468   Belikovich, M. V., Kulikov, M. Yu., Nechaev, A. A., Feigin, A. M.: Evaluation of the

469   Atmospheric Minor Species Measurements: a Priori Statistical Constraints Based on

470   Photochemical Modeling, Radiophys. Quantum Electron., 61, 574-588, doi:10.1007/s11141-

471   019-09918-5, 2018.

472

473   Berger, U.: Modeling of the middle atmosphere dynamics with LIMA, J. Atmos. Terr. Phys.,

474   70, 1170–1200, doi:10.1016/j.jastp.2008.02.004, 2008.

475

476   Bittner, M., Offermann, D., Graef, H.-H., Donner, M., and Hamilton, K.: An 18 year time

477   series of OH rotational temperatures and middle atmosphere decadal variations, J. Atmos. Sol.

478   Terr. Phys., 64, 1147-1166, doi:10.1016/S1364-6826(02)00065-2, 2002.

479

480   Buriti, R. A., Takahashi, H., Lima, L. M., and Medeiros, A. F.: Equatorial planetary waves in

481   the mesosphere observed by airglow periodic oscillations, Adv. Space Res., 35, 2031–2036,

482   doi:10.1016/j.asr.2005.07.012, 2005.

483

484 Burkholder, J. B., Sander, S. P., Abbatt, J., Barker, J. R., Huie, R. E., Kolb, C. E., Kurylo, M.

485 J., Orkin, V. L., Wilmouth, D. M., and Wine, P. H.: Chemical Kinetics and Photochemical

486 Data for Use in Atmospheric Studies, Evaluation No. 18, JPL Publication 15-10, Jet

487 Propulsion Laboratory, Pasadena, http://jpldataeval.jpl.nasa.gov, 2015.

488

489 Caridade, P. J. S. B., Horta, J.-Z. J., and Varandas, A. J. C.: Implications of the O + OH

490 reaction in hydroxyl nightglow modeling, Atmos. Chem. Phys., 13, 1-13, doi:10.5194/acp-13-

491 1-2013, 2013.

492

493 Dalin, P., Perminov, V., Pertsev, N., and Romejko, V.: Updated long-term trends in

494 mesopause temperature, airglow emissions, and noctilucent clouds, J. Geophys. Res. Atmos.,

495 125, e2019JD030814, doi:10.1029/2019JD030814, 2020.

496

497 Damiani, A., Storini, M., Santee, M. L., and Wang, S.: Variability of the nighttime OH layer

498 and mesospheric ozone at high latitudes during northern winter: influence of meteorology,

499 Atmos. Chem. Phys., 10, 10291-10303, doi:10.5194/acp-10-10291-2010, 2010.

500

501 Gao, H., Xu, J., and Wu, Q.: Seasonal and QBO variations in the OH nightglow emission

502 observed by TIMED/SABER, J. Geophys. Res., 115, A06313, doi:10.1029/2009JA014641,

503 2010.

504

505 Gao, H., Xu, J., Ward, W., and Smith, A. K.: Temporal evolution of nightglow emission

506 responses to SSW events observed by TIMED/SABER, J. Geophys. Res., 116, D19110,

507 doi:10.1029/2011JD015936, 2011.

508

509 Garcia, R. R., and Solomon, S.: The effect of breaking gravity waves on the dynamics and

510 chemical composition of the mesosphere and lower thermosphere, J. Geophys. Res., 90(D2),

511 3850–3868, doi:10.1029/JD090iD02p03850, 1985.

512

513 Good, R. E.: Determination of atomic oxygen density from rocket borne measurements of

514 hydroxyl airglow, Planet. Space Sci., 24, 389–395, doi:10.1016/0032-0633(76)90052-0, 1976.

515

516 Grygalashvyly, M., Sonnemann, G. R., Lübken, F.-J., Hartogh, P., and Berger, U.: Hydroxyl

517 layer: Mean state and trends at midlatitudes, J. Geophys. Res., 119, 12391–12419,

518 doi:10.1002/2014JD022094, 2014.

519

520 Grygalashvyly, M.: Several notes on the OH*-layer, Ann. Geophys., 33, 923-930,

521 doi:10.5194/angeo-33-923-2015, 2015.

522

523 Grygalashvyly, M., and Sonnemann, G. R.: Note on Consistency between Kalogerakis-

524 Sharma Mechanism (KSM) and Two-Step Mechanism of Atmospheric Band Emission, Earth

525 Planets Space, 72(187), doi:10.1186/s40623-020-01321-z, 2020.

526

527 Hartogh, P., Sonnemann, G. R., Grygalashvyly, M., Li, S., Berger, U., and Lübken, F.-J.:

528 Water vapor measurements at ALOMAR over a solar cycle compared with model calculations

529 by LIMA, J. Geophys. Res., 114, doi:10.1029/2009JD012364, 2010.

530

531 Hartogh, P., Jarchow, C., Sonnemann, G. R., and Grygalashvyly, M.: Ozone distribution in

532 the middle latitude mesosphere as derived from microwave measurements at Lindau (51.66°

533 N, 10.13° E), J. Geophys. Res., 116, D04305, doi:10.1029/2010JD014393, 2011.

534

535   Holmen, S. E., Dyrland, M. E., and Sigernes, F.: Long-term trends and the effect of solar

536   cycle variations on mesospheric winter temperatures over Longyearbyen, Svalbard (78°N), J.

537   Geophys. Res. Atmos., 119, 6596–6608, doi:10.1002/2013JD021195, 2014.

538

539   Kalicinsky, C., Knieling, P., Koppmann, R., Offermann, D., Steinbrecht, W., and Wintel, J.:

540   Long-term dynamics of OH* temperatures over central Europe: trends and solar correlations,

541   Atmos. Chem. Phys., 16, 15033-15047, doi:10.5194/acp-16-15033-2016, 2016.

542

543   Kaye, J. A.: On the possible role of the reaction $O + HO_2 \rightarrow OH + O_2$ in OH airglow, J.

544   Geophys. Res., 93, 285–288, doi:10.1029/JA093iA01p00285, 1988.

545

546   Kremp, Ch., Berger, U., Hoffmann, P., Keuer, D., and Sonnemann, G. R.: Seasonal variation

547   of middle latitude wind fields of the mesopause region -a comparison between observation

548   and model calculation, Geophys. Res. Lett., 26, 1279-1282, doi:10.1029/1999GL900218,

549   1999.

550

551   Kulikov, M. Y., Feigin, A. M., and Sonnemann, G. R.: Retrieval of water vapor profile in the

552   mesosphere from satellite ozone and hydroxyl measurements by the basic dynamic model of

553   mesospheric photochemical system, Atmos. Chem. Phys., 9, 8199–8210, doi:10.5194/acp-9-

554   8199-2009, 2009.

555

556   Kulikov, M. Yu., Belikovich, M. V., Grygalashvyly, M., Sonnemann, G. R., Ermakova, T. S.,

557   Nechaev, A. A., and Feigin, A. M.: Nighttime ozone chemical equilibrium in the mesopause

558   region, J. Geophys. Res., 123, 3228-3242, doi:10.1002/2017JD026717, 2018.

559

560 Kulikov, M. Yu., Belikovich, M. V., Ermakova, T. S., Nechaev, A. A., and Feigin, A. M.:

561 Technical note: Evaluation of the simultaneous measurements of mesospheric OH, HO_2, and

562 O_3 under a photochemical equilibrium assumption – a statistical approach, Atmos. Chem.

563 Phys., 18, 7453–7471, doi:10.5194/acp-18-7453-2018, 2018.

564

565 Kulikov, M. Yu., Nechaev, A. A. , Belikovich, M. V., Vorobeva, E. V., Grygalashvyly, M.,

566 Sonnemann, G. R., and Feigin, A. M.: Boundary of Nighttime Ozone Chemical Equilibrium

567 in the Mesopause Region from SABER Data: Implications for Derivation of Atomic Oxygen

568 and Atomic Hydrogen, Gepohys. Res. Lett., 46, 997-1004, doi:10.1029/2018GL080364,

569 2019.

570

571 Le Texier, H., Solomon, S., and Garcia, R. R.: Seasonal variability of the OH Meinel bands,

572 Planet. Space Sci., 35(8), 977-989, doi:10.1016/0032-0633(87)90002-X, 1987.

573

574 Limpasuvan, V., Richter, J. H., Orsolini, Y. J., Stordal, F., and Kvissel, O.-K.: The roles of

575 planetary and gravity waves during a major stratospheric sudden warming as characterized by

576 WACCM, J. Atmos. Sol. Terr. Phys., 78–79, 84–98, doi:10.1016/j.jastp.2011.03.004, 2012.

577

578 Limpasuvan, V., Orsolini, Y. J., Chandran, A., Garcia, R. R., and Smith, A. K.: On the

579 composite response of the MLT to major sudden stratospheric warming events with elevated

580 stratopause, J. Geophys. Res. Atmos., 121, 4518–4537, doi:10.1002/2015JD024401, 2016.

581

582 Liu, G., and Shepherd, G. G.: An empirical model for the altitude of the OH nightglow

583 emission, Geophys. Res. Lett., 33, L09805, doi:10.1029/2005GL025297, 2006.

584

585   Liu, G., Shepherd, G. G., and Roble, R. G.: Seasonal variations of the nighttime O(^{1}S) and

586   OH airglow emission rates at mid-to-high latitudes in the context of the large-scale

587   circulation, J. Geophys. Res., 113, A06302, doi:10.1029/2007JA012854, 2008.

588

589   Lopez-Gonzalez, M. J., Rodriguez, E., Wiens, R. H., Shepherd, G. G., Sargoytchev, S.,

590   Brown, S., Shepherd, M. G., Aushev, V. M., Lopez-Moreno, J. J., Rodrigo, R., and Cho, Y.-

591   M.: Seasonal variations of O_2 atmospheric and OH(6–2) airglow and temperature at mid-

592   latitudes from SATI observations, Ann. Geophys., 22, 819–828, doi:10.5194/angeo-22-819-

593   2004, 2004.

594

595   Lopez-Gonzalez, M. J., Rodriguez, E., Shepherd, G. G., Sargoytchev, S., Shepherd, M. G.,

596   Aushev, V. M., Brown, S., Garcia-Comas, M., and Wiens, R. H.: Tidal variations of O_2

597   Atmospheric and OH(6-2) airglow and temperature at mid-latitudes from SATI observations,

598   Ann. Geophys., 23, 3579–3590, doi:10.5194/angeo-23-3579-2005, 2005.

599

600   Lopez-Gonzalez, M. J., Garcia-Comas, M., Rodriguez, E., Lopez-Puertas, M., Shepherd, M.

601   G., Shepherd, G. G., Sargoytchev, S., Aushev, V. M., Smith, S. M., Mlynczak, M. G.,

602   Russell, J. M., Brown, S., Cho, Y.-M., and Wiens, R. H.: Ground-based mesospheric

603   temperatures at mid-latitude derived from O_2 and OH (6-2) airglow SATI data: Comparison

604   with SABER measurements, J. Atmos. Solar-Terr. Phys., 69, 2379–2390.

605   doi:10.1016/j.jastp.2007.07.004, 2007.

606

607   Lopez-Gonzalez, M. J., Rodríguez, E., Garcia-Comas, M., Costa, V., Shepherd, M. G.,

608   Shepherd, G. G., Aushev, V. M., and Sargoytchev, S.: Climatology of planetary wave type

609   oscillations with periods of 2–20 days derived from O_2 atmospheric and OH(6-2) airglow

observations at mid-latitude with SATI, Ann.Geophys., 27, 3645–3662, doi:10.5194/angeo-27-3645-2009, 2009.

Lübken, F.-J., Berger, U., and Baumgarten, G.: Stratospheric and solar cycle effects on long-term variability of mesospheric ice clouds, J. Geophys. Res., 114, D00106, doi:10.1029/2009JD012377, 2009.

Lübken, F.-J., Berger, U., and Baumgarten, G.: Temperature trends in the midlatitude summer mesosphere, J. Geophys. Res., 118, 13347-13360, doi:10.1002/2013JD020576, 2013.

Makhlouf, U. B., Picard, R. H., and Winick, J. R.: Photochemical-dynamical modeling of the measured response of airglow to gravity waves. 1. Basic model for OH airglow, J. Geophys. Res., 100, 11289–11311, doi:10.1029/94JD03327, 1995.

Marsh, D. R., Smith, A. K., Mlynczak, M. G., and Russell III, J. M.: SABER observations of the OH Meinel airglow variability near the mesopause, J. Geophys. Res., 111, A10S05, doi:10.1029/2005JA011451, 2006.

Mlynczak, M. G., Hunt, L. A., Mast, J. C., Marshall, B. T., Russell III, J. M., Smith, A. K., Siskind, D. E., Yee, J.-H., Mertens, C. J., Martin-Torres, F. J., Thompson, R. E., Drob, D. P., and Gordley, L. L.: Atomic oxygen in the mesosphere and lower thermosphere derived from SABER: Algorithm theoretical basis and measurement uncertainty, J. Geophys. Res. Atmos., 118, 5724–5735, doi:10.1002/jgrd.50401, 2013a.

Mlynczak, M. G., Hunt, L. A., Mertens, C. J., Marshall, B. T., Russell III, J. M., Lopez-Puertas, M., Smith, A. K., Siskind, D. E., Mast, J. C., Thompson, R. E., and Gordley, L. L.:

636 Radiative and energetic constraints on the global annual mean atomic oxygen concentration in

637 the mesopause region, J. Geophys. Res. Atmos., 118, 5796–5802, doi:10.1002/jgrd.50400,

638 2013b.

639

640 Mlynczak, M. G., Hunt, L. A., Marshall, B. T., Mertens, C. J., Marsh, D. R., Smith, A. K.,

641 Russell, J. M., Siskind, D. E., and Gordley, L. L.: Atomic hydrogen in the mesopause region

642 derived from SABER: Algorithm theoretical basis, measurement uncertainty, and results, J.

643 Geophys. Res., 119, 3516–3526, doi:10.1002/2013JD021263, 2014.

644

645 Morton, K. W., and D. F. Mayers, D. F.: Numerical Solution of Partial Differential Equations,

646 Cambridge University Press, 1994.

647

648 Pertsev N. N., Andreyev A. B., Merzlyakov E. G., and Perminov V. I.: Mesosphere-

649 thermosphere manifestations of strato-spheric warmings: joint use of satellite and ground-

650 based measurements, Current Problems in Remote Sensing of the Earth from Space, 10(1),

651 93–100, http://jr.rse.cosmos.ru/article.aspx?id=1154&lang=eng, 2013.

652

653 Popov, A. A., Gavrilov, N. M., Andreev, A. B., and Pogoreltsev, A. I.: Interannual dynamics

654 in intensity of mesoscale hydroxyl nightglow variations over Almaty, Solar-Terr. Phys., 4(2),

655 63–68, doi:/10.12737/stp-42201810, 2018.

656

657 Popov, A. A., Gavrilov, N. M., Perminov, V. I., Pertsev, N. N., and Medvedeva, I. V.: Multi-

658 year observations of mesoscale variances of hydroxyl nightglow near the mesopause at Tory

659 and Zvenigorod, J. Atmos. Solar-Terr. Phys., 205, 1-8, doi:10.1016/j.jastp.2020.105311,

660 2020.

661

662   Reid, I. M., Spargo, A. J., and Woithe, J. M.: Seasonal variations of the nighttime O(^{1}S) and

663   OH (8-3) airglow intensity at Adelaide, Australia, J. Geophys. Res. Atmos., 119, 6991–7013,

664   doi:10.1002/2013JD020906, 2014.

665

666   Reid, I. M., Spargo, A. J., Woithe, J. M., Klekociuk, A. R., Younger, J. P., and G. G. Sivjee,

667   G. G.: Seasonal MLT-region nightglow intensities, temperatures, and emission heights at a

668   Southern Hemisphere midlatitude site, Ann. Geophys., 35, 567-582, doi:10.5194/angeo-35-

669   567-2017, 2017.

670

671   Reisin, E., Scheer, J., Dyrland, M. E., Sigernes, F., Deehr, C. S., Schmidt, C., Höppner, K.,

672   Bittner, M., Ammosov, P. P., Gavrilyeva, G. A., Stegman, J., Perminov, V. I., Semenov, A. I.,

673   Knlieling, P., Koomann, R., Shiokawa, K., Lowe, R. P., Lopez-Gonzalez, M. J., Rodriguez,

674   E., Zhao, Y., Taylor, M. J., Buriti, R. A., Espy, P. E., French, W. J., Eichmann, K.-U.,

675   Burrows, J. P., and von Savigny, C.: Traveling planetary wave activity from mesopause

676   region airglow temperatures determined by the Network for the Detection of Mesospheric

677   Change (NDMC), J. Atmos. Sol.-Terr. Phys., 119, 71–82, doi:10.1016/j.jastp.2014.07.002,

678   2014.

679

680   Russell, J. P., Ward, W. E., Lowe, R. P., Roble, R. G., Shepherd, G. G., and B. Solheim, B.:

681   Atomic oxygen profiles (80 to 115 km) derived from Wind Imaging Interferometer/Upper

682   Atmospheric Research Satellite measurements of the hydroxyl and greenline airglow: Local

683   time–latitude dependence, J. Geophys. Res., 110, D15305, doi:10.1029/2004JD005570, 2005.

684

685   Shepherd, G. G., Thuillier, G., Cho, Y.-M., Duboin, M.-L., Evans, W. F. J., Gault, W. A.,

686   Hersom, C., Kendall, D. J. W., Lathuillère, C., Lowe, R. P., McDade, I. C., Rochon, Y. J.,

687   Shepherd, M. G., Solheim, B. H., Wang, D.-Y., and Ward, W. E.: The Wind Imaging

688   Interferometer (WINDII) on the Upper Atmosphere Research Satellite: A 20 year perspective,

689   Rev. Geophys., 50, RG2007, doi:10.1029/2012RG000390, 2012.

690

691   Shepherd, M. G., Cho, Y.-M., Shepherd, G. G., Ward, W., and Drummond, J. R.:

692   Mesospheric temperature and atomic oxygen response during the January 2009 major

693   stratospheric warming, J. Geophys. Res., 115, A07318, doi:10.1029/2009JA015172, 2010.

694

695   Shimazaki, T.: Minor constituents in the middle atmosphere, D. Reidel Publishing Company,

696   Dordrecht, Holland, 1985.

697

698   Smith, A. K., Marsh, D. R., Russell III, J. M., Mlynczak, M. G., Martin-Torres, F. J., and

699   Kyrölä, E.: Satellite observations of high nighttime ozone at the equatorial mesopause, J.

700   Geophys. Res., 113, D17312, doi:10.1029/2008JD010066, 2008.

701

702   Smith, A. K., Lopez-Puertas, M., Garcia-Comas, M., and Tukiainen, S.: SABER observations

703   of mesospheric ozone during NH late winter 2002-2009, Geophys. Res. Lett., 36, L23804,

704   doi:10.1029/2009GL040942, 2009.

705

706   Smith, A. K., Marsh, D. R., Mlynczak, M. G., and Mast, J. C.: Temporal variation of atomic

707   oxygen in the upper mesosphere from SABER, J. Geophys. Res., 115, D18309,

708   doi:10.1029/2009JD013434, 2010.

709

710   Sonnemann, G. R., Hartogh, P., Jarchow., C., Grygalashvyly, M., and Berger, U.: On the

711   winter anomaly of the night-to-day ratio of ozone in the middle to upper mesosphere in

712   middle to high latitudes, Adv. Space Res., 40, 846-854, doi:10.1016/j.asr.2007.01.039, 2007.

713

714   Sonnemann, G. R., Hartogh, P., Grygalashvyly, M., Li, S., and Berger, U.: The quasi 5-day

715   signal in the mesospheric water vapor concentration in high latitudes in 2003 - a comparison

716   between observations at ALOMAR and calculations, J. Geophys. Res., 113, D04101,

717   doi:10.1029/2007JD008875, 2008.

718

719   Sonnemann, G. R., Hartogh, P., Berger, U., and Grygalashvyly, M.: Hydroxyl layer: trend of

720   number density and intra-annual variability, Ann. Geophys., 33, 749–767, doi:10.5194/angeo-

721   33-749-2015, 2015.

722

723   Sonnemann G., and Grygalashvyly, M.: The slow-down effect in the nighttime mesospheric

724   chemistry of hydrogen radicals, Adv. Space Res., 65, 2800-2807,

725   doi:10.1016/j.asr.2020.03.025, 2020.

726

727   Takahashi, H., and Batista, P. P.: Simultaneous measurements of OH (9,4), (8,3), (7,2), 6,2),

728   and (5,1) bands in the airglow, J. Geophys. Res., 86, 5632–5642,

729   doi:10.1029/JA086iA07p05632, 1981.

730

731   Takahashi, H., Clemesha, B. R., and Batista, P. P.: Predominant semi-annual oscillation of the

732   upper mesospheric airglow intensities and temperatures in the equatorial region, J. Atmos.

733   Terr. Phys., 57(4), 407-414, doi:10.1016/0021-9169(94)E0006-9, 1995.

734

735   Takahashi, H., Batista, P. P., Buriti, R. A, Gobbi, D., Nakamura, T., Tsuda, T., and Fukao, S.:

736   Response of the airglow OH emission, temperature and mesopause wind to the atmospheric

737   wave propagation over Shigaraki, Japan, Earth Planets Space, 51, 863–875,

738   doi:10.1186/BF03353245, 1999.

739

740 Taylor, M. J., Espy, P. J., Baker, D. J., Sica, R. J., Neal, P. C., and Pendleton, Jr. W. R.:

741 Simultaneous intensity, temperature and imaging measurements of short period wave

742 structure in the OH nightglow emission, Planet. Space Sci., 39, 1171–1188,

743 doi:10.1016/0032-0633(91)90169-B, 1991.

744

745 Varandas, A. J. C.: Reactive and non-reactive vibrational quenching in O + OH collisions,

746 Chem. Phys. Lett., 396, 182–190, doi:10.1016/j.cplett.2004.08.023, 2004.

747

748 Wachter, P., Schmidt, C., Wüst, S., and Bittner, M.: Spatial gravity wave characteristics

749 obtained from multiple OH(3-1) airglow temperature time series, J. Atmos. Sol. Terr. Phys.,

750 135, 192-201, doi:10.1016/j.jastp.2015.11.008, 2015.

751

752 Walcek, C. J.: Minor flux adjustment near mixing ratio extremes for simplified yet highly

753 accurate monotonic calculation of tracer advection, J. Geophys. Res., 105, 9335-9348,

754 doi:10.1029/1999JD901142, 2000.

755

756 Wiens, R. H., Moise, A., Brown, S., Sargoytchev, S., Peterson, R. N., Shepherd, G. G.,

757 Lopez-Gonzalez, M. J., Lopez-Moreno J. J., and Rodrigo R.: SATI: A spectral airglow

758 tempera-ture imager, Adv. Space Res. 1997, 19, 677–680, doi:10.1016/S0273-

759 1177(97)00162-2, 1997.

760

761 Xu, J., Smith, A. K., Jiang, G., Gao, H., Wei, Y., Mlynczak, M. G., and Russell III, J. M.:

762 Strong longitudinal variations in the OH nightglow, Geophys. Res. Lett., 37, L21801,

763 doi:10.1029/2010GL043972, 2010.

764

765 Xu, J., Gao, H., Smith, A. K., and Zhu, Y.: Using TIMED/SABER nightglow observations to

766 investigate hydroxyl emission mechanisms in the mesopause region, J. Geophys. Res., 117,

767 D02301, doi:10.1029/2011JD016342, 2012.

768

769

770

771

772

773

774

775

776

777

778

779

780

781

782

783

784

785

786

787

788

789 **Table 1**. List of reactions with corresponding reaction rates (for three-body reactions [cm^6

790 molecule^{-2} s^{-1}] and for two-body reactions [cm^3 molecule^{-1} s^{-1}]), branching ratios, quenching

791 coefficients, and spontaneous emission coefficients (s^{-1}) used in the paper.

	Reaction	Coefficient/branching ratios	Reference
1	$H + O_3 \xrightarrow{\varsigma_v a_1} OH_{v=5,\dots,9} + O_2$	$a_1 = 1.4 \cdot 10^{-10} exp\left(\frac{-470}{T}\right)$ $\varsigma_{v=9,\dots,5} = 0.47, 0.34, 0.15, 0.03, 0.01$	Burkholder et al. (2015), Adler-Golden (1997)
2	$O + HO_2 \xrightarrow{\psi_v a_2} OH_{v=5,\dots,9} + O_2$	$a_2 = 3.0 \cdot 10^{-11} exp\left(\frac{200}{T}\right)$ $\psi_{v=3,\dots,1} = 0.1, 0.13, 0.34$	Burkholder et al. (2015), Kaye (1988), Takahashi and Batista (1981)
3	$O + OH_{v=1,\dots,9} \rightarrow O_2 + H$	$a_3(v = 9, \dots, 5) = (5.07, 4.52, 3.87, 3.93, 3.22, 3.68, 3.05, 3.19, 3,42) \cdot 10^{-11}$	Varandas (2004), Caridade et al. (2013)
4	$O + O_2 + M \rightarrow O_3 + M$	$a_4 = 6 \cdot 10^{-34}(300/T)^{2.4}$	Burkholder et al. (2015)
5	$O + O_3 \rightarrow 2O_2$	$a_5 = 8 \cdot 10^{-12} exp\left(\frac{-2060}{T}\right)$	Burkholder et al. (2015)
6	$OH_v + O_2, O, N_2 \rightarrow OH_{v'<v} + O_2, O, N_2$	$B_{vv'}, D_{vv'}, C_{vv'}$	Adler-Golden (1997), Caridade et al. (2013), Makhlouf et al. (1995)
7	$OH_v \rightarrow OH_{v'<v} + hv$	$E_{vv'}$	Xu et al. (2012)

792

793

794

795
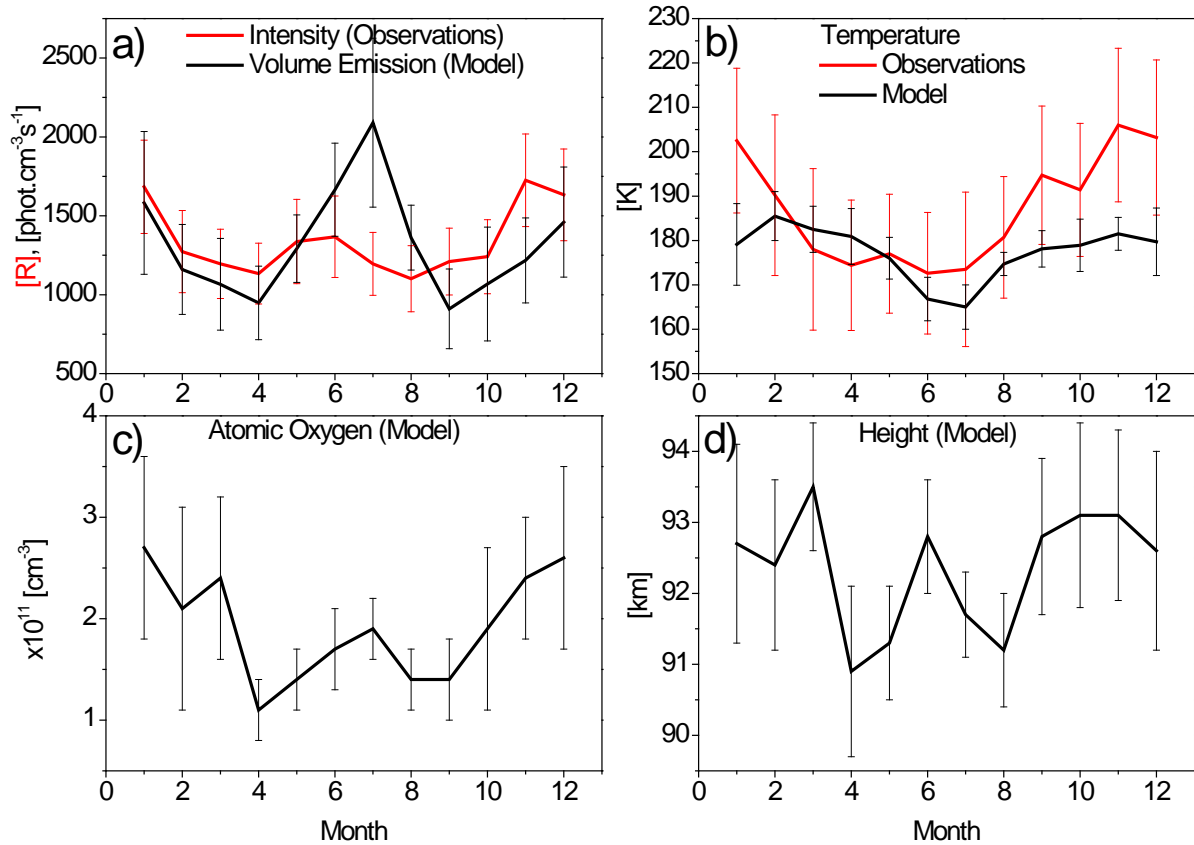
796

797

798

799

800

801

802

803

804

805

Figures

807   Figure 1. Observed at 43° N (~~black~~ red line) and modelled at 43.75° N (~~red~~ black line), annual

808   variability of intensity and volume emission (a), temperature (b), atomic oxygen

809   concentration (c), and height at the peak of the $OH^*_{v=6}$ layer.
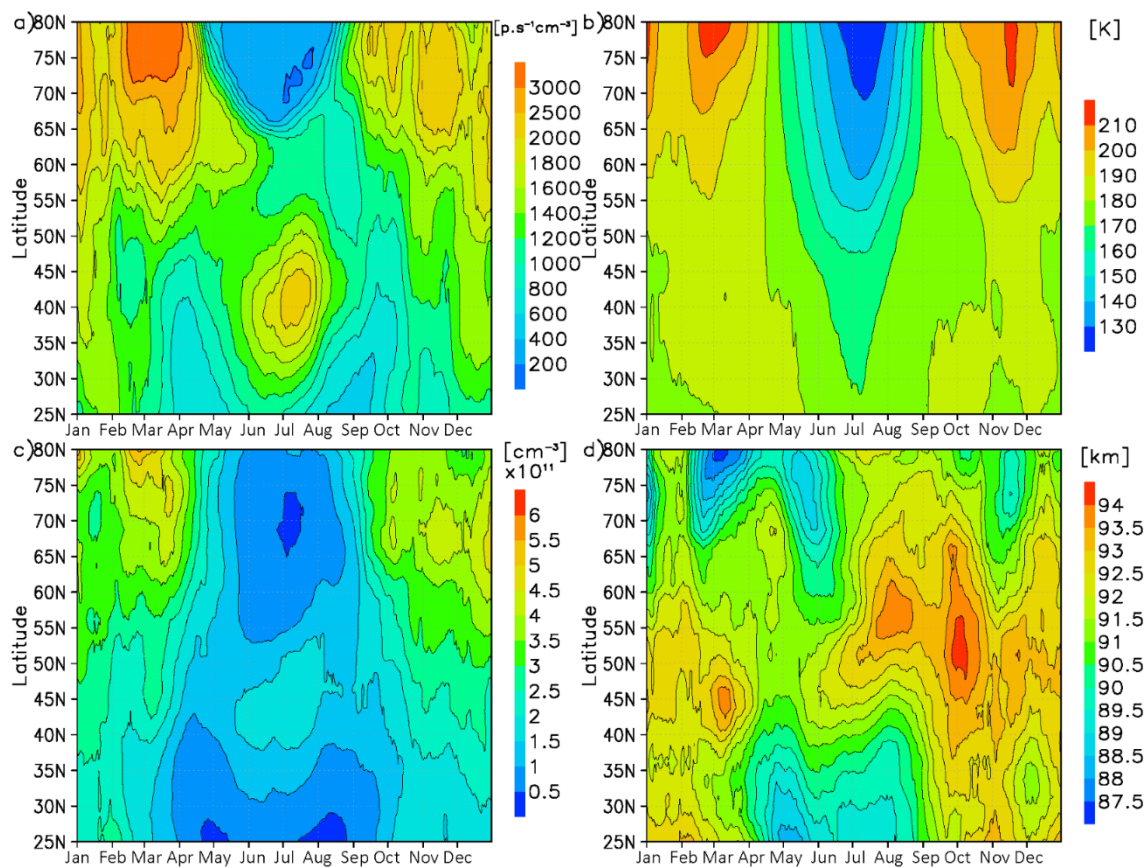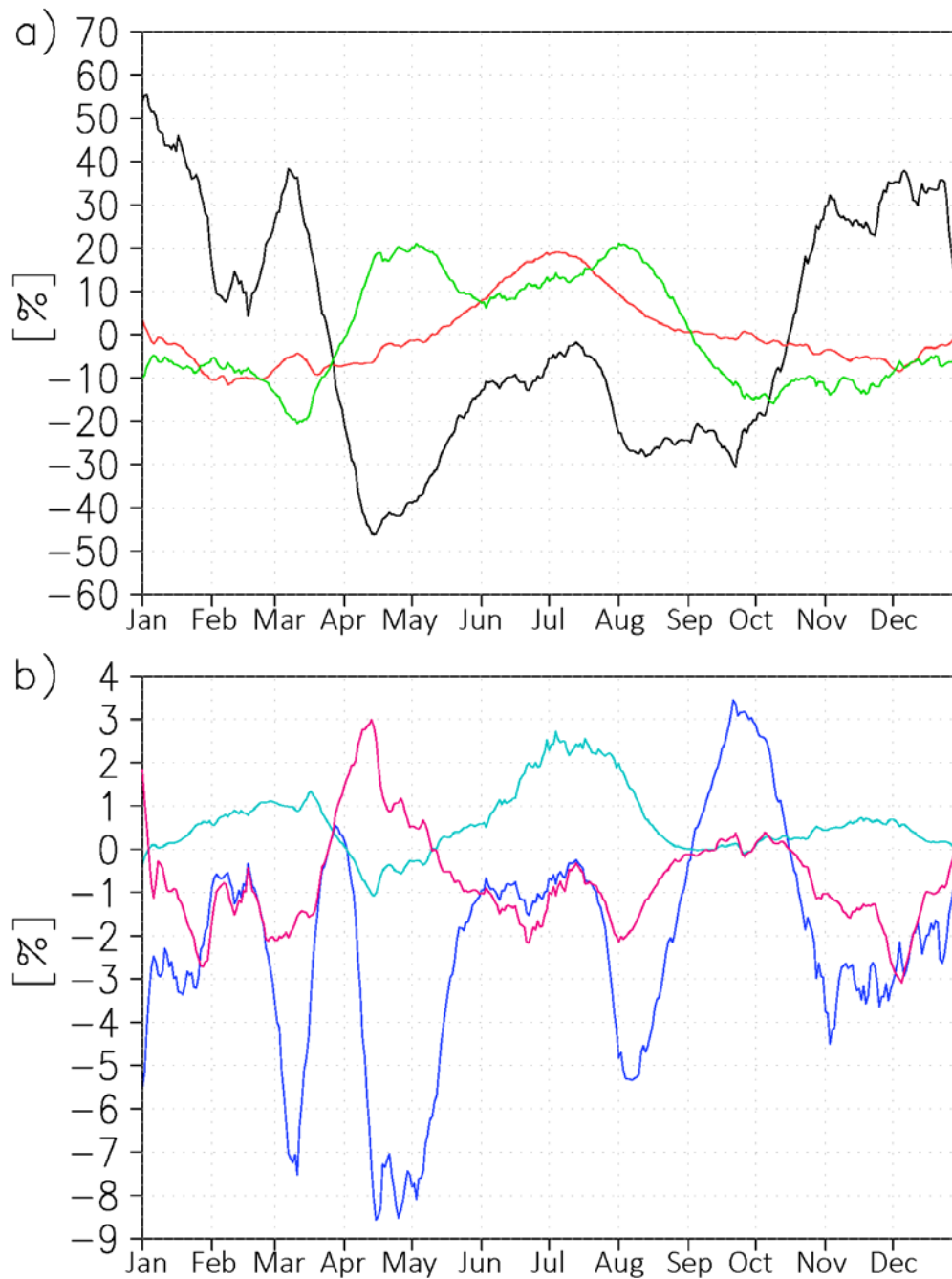

810

811

812

813

814

815

816

817

818

819

820

821   Figure 2. Nightly mean one-month sliding average volume emission (a), temperature (b),

822   atomic oxygen at peak of $OH^*_{v=6}$ (c), and height of peak of $OH^*_{v=6}$.

823

824

825

826

827

828

829

830

831

832

Figure 3. a) relative to annual averaged variations of volume emission (Eq. 2) due to atomic oxygen (black line), temperature (red line), and height (green line) at 43.75° N, b) relative variations of volume emissions due to second momentum $\frac{[O]'M'}{[O]\bar{M}}$ (blue line), $\frac{T'M'}{\bar{T}\bar{M}}$ (cyan line), and $\frac{[O]'T'}{[O]\bar{T}}$ (magenta line) at 43.75° N.